Article
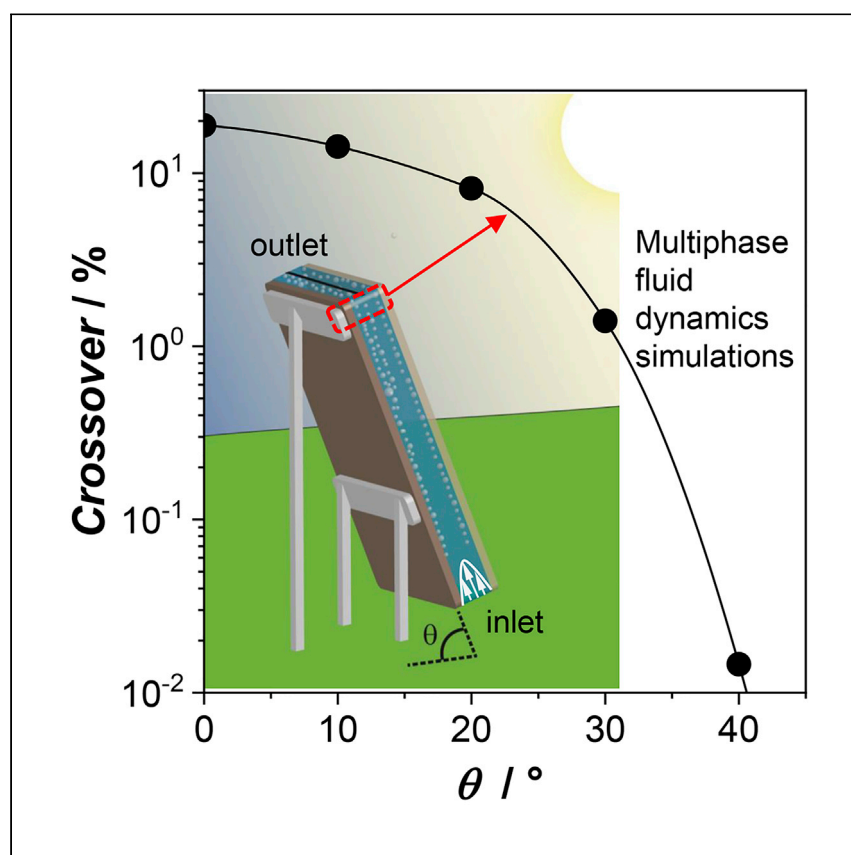
Multiphase fluid dynamics simulations of product crossover in solar-driven, membrane-less water splitting

Keisuke Obata, Amel Mokeddem, Fatwa F. Abdi

keisuke.obata@helmholtz-berlin.de (K.O.)
fatwa.abdi@helmholtz-berlin.de (F.F.A.)

HIGHLIGHTS

Multiphase fluid dynamics simulations are introduced for solar-driven water splitting

Device orientation and bubbles characteristics are essential for product separation

A universal design guideline based on dimensionless numbers is proposed

Hydrodynamic control in a (photo)electrochemical water-splitting device potentially allows product gas separation without any separators between the electrodes. Obata et al. introduce multiphase fluid dynamics simulations, which highlight the significance of bubbles and controlling their formation for efficient product gas collection in solar-driven water splitting.

Article

Multiphase fluid dynamics simulations of product crossover in solar-driven, membrane-less water splitting

Keisuke Obata,[1,*] Amel Mokeddem,[1,2] and Fatwa F. Abdi[1,3,4,*]

SUMMARY

Efficient separation of product gases is essential for the safe operation of large-scale, solar-driven water-splitting devices. To date, most demonstration devices use membranes, but a membrane-less configuration that separates products via hydrodynamic control offers an attractive alternative without the complexity associated with using membranes. In the present study, multiphase fluid dynamics simulations are introduced to investigate product crossover in a membrane-less, solar-driven water-splitting device. Specific emphasis is placed on implementing a realistic tilt condition of the device and the buoyancy effects on product gas bubbles. Our simulations reveal that gas bubbles, often disregarded, can be a major source of crossover rather than dissolved gases. Controlling the bubble formation and characteristics (e.g., diameter) therefore plays an important role in achieving efficient product separation. Finally, universal design criteria to control the product crossover are further discussed based on dimensionless analysis.

INTRODUCTION

In solar-driven water splitting, tremendous efforts have been devoted to the development of efficient light-absorbing semiconductors and electrocatalysts as the key components. As a result, various demonstration devices with solar-to-hydrogen efficiencies (η_{STH}) well above 10% have been reported.[1–4] Among these devices, various approaches exist. For instance, photovoltaic (PV) panels can be connected to electrolyzers (EC) to indirectly convert solar electricity to hydrogen (PV-EC). In this approach, sunlight absorption to generate electrons and electrochemical processes occur at two different physical sites, i.e., PV and electrolyzer, respectively. Alternatively, a photoelectrochemical (PEC) approach, in which semiconductors—often decorated with additional co-catalysts—are directly immersed in the electrolyte as photoelectrodes, offers several advantages. For example, because light absorption and electrochemistry are integrated into a single device, the infrared photons of solar irradiation that are not absorbed by the semiconductor can heat the system, thereby improving catalytic reaction kinetics, mass transport, and ionic conductivity in the electrolyte.[5–12] When oxide semiconductors are used, charge carrier transport may also be improved at elevated temperatures.[13–16] Moreover, the 10–100× lower current density in the PEC versus the PV-EC approach potentially allows the use of semiconductors and catalysts based on earth-abundant materials. Note that the photoelectrodes used in the PEC approach can also be fabricated by integrating photovoltaic materials and electrocatalysts used in the PV-EC approach.

At this stage of the development, reactor engineering plays an important role to fully utilize and translate the materials and devices developed in laboratories for practical

[1]Institute for Solar Fuels, Helmholtz-Zentrum Berlin für Materialien und Energie GmbH, Hahn-Meitner-Platz 1, 14109 Berlin, Germany

[2]Department of Thermal and Energy Engineering, Polytech de Nantes, 2 Rue Christian Pauc, 44300 Nantes, France

[3]Twitter: @fatwafirdaus

[4]Lead contact

*Correspondence:
keisuke.obata@helmholtz-berlin.de (K.O.),
fatwa.abdi@helmholtz-berlin.de (F.F.A.)

large-scale applications. In addition to having a high η_{STH}, a safe and efficient separation of products is critical in a solar-driven water-splitting device. In the PEC approach, the oxidation and reduction reactions occur at two completely isolated electrodes, i.e., the anode and cathode, respectively. To avoid forming an explosive mixture of product gases (i.e., H_2 and O_2), an ion exchange membrane or a diaphragm is often employed as a separator between the anode and the cathode in lab-scale devices. However, implementing separators poses additional complexity. Also, the separators often suffer from degradation during long-term operation due to cationic impurities in the electrolyte.[17] Alternatively, a membrane-less configuration has been proposed.[17,18] By controlling the hydrodynamics of the device, H_2 and O_2 can be collected from the outlet before they get mixed in the electrolyte without any separators. This membrane-less architecture has been demonstrated in a variety of electrochemical devices, such as water electrolyzers, fuel cells, and redox flow batteries.[19–28]

Several studies have investigated the product crossover in membrane-less electrochemical water-splitting devices. For example, the distribution of dissolved product gases in laminar flow has been simulated,[29–32] and the electrolyte flow rate and device geometry were shown to determine the effectiveness of product separation. However, these simulations only considered the transport of diluted species (i.e., dissolved gases) and assumed no product gas bubbles. In addition, most reports only considered devices oriented vertically. No study has investigated the influence of the tilt position of the device on the product crossover, which may largely depend on the buoyancy effects on gas bubbles. This is particularly important in solar-driven water splitting with the PEC approach because the devices have to be inevitably tilted to achieve the maximum efficiency. As is the case for fixed PV panels, the optimal angle largely depends on the location (e.g., ~30° from horizontal in Europe).[33] This optimal angle is expected to be the same for PEC water-splitting devices in terms of current or product generation, but not necessarily the case in terms of product separation.

In the present study, Euler-Euler multiphase fluid dynamics simulations are performed to identify the contribution of product gas bubbles to the overall product crossover in a membrane-less water-splitting device tilted from the horizontal orientation. As frequently applied in modeling electrochemical gas-producing reactions,[34–38] Euler-Euler model simulates the volume fractions and velocity vectors of the dispersed and continuous phases from two sets of continuity and momentum equations without being too computationally expensive, as is the case for direct numerical simulation or Euler-Lagrange method.[21,39–42] Based on our simulations, we will show that gas bubbles play a more significant role than dissolved gases in determining product crossover in membrane-less devices. The nature of gas bubbles and its influence on the overall product separation are also further discussed. Finally, governing dimensionless numbers are derived to obtain universal descriptors for the design of efficient membrane-less, solar-driven water-splitting devices.

RESULTS AND DISCUSSION

Product crossover in solar-driven, membrane-less water-splitting devices

Our multiphase fluid dynamics simulations are largely inspired by the reports from the group of Mahmut D. Mat, in which they validated their model with the gas volume fractions estimated from the local conductivity measurements during water splitting with vertically oriented electrodes.[35–37] A schematic representation of our model and the accompanying boundary conditions are shown in Figure S1. Further
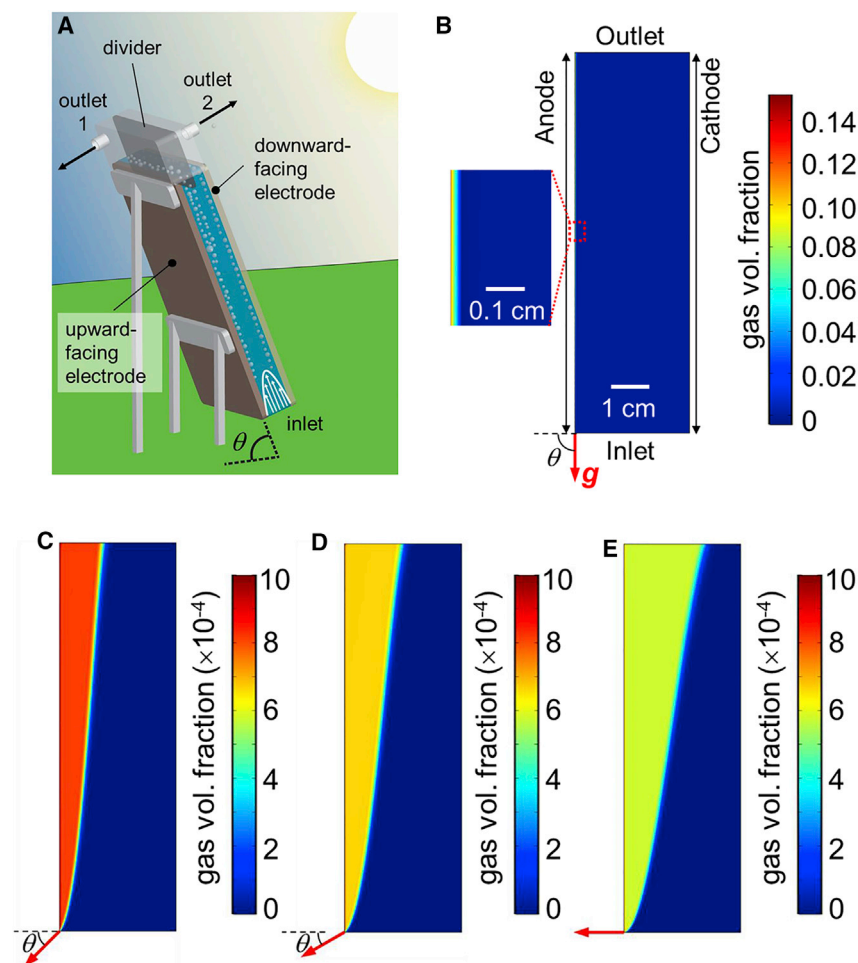
Figure 1. Schematic illustration of the simulated device and volume fraction of product O$_2$ bubbles with various orientations

(A) Schematic illustration of the simulated device.

(B–E) Colormaps of the simulated volume fraction of O$_2$ bubbles for devices with θ = (B) 90° (vertical orientation), (C) 45°, (D) 30°, and (E) 0° (horizontal orientation). The red arrows indicate the direction of gravity in each case. The inset in (B) indicates the magnification of the colormap at regions very close to the anode. In all cases, the average liquid inlet velocity is 2.5 cm s^{-1}, the average current density is 10 mA cm^{-2}, the bubble diameter is 0.1 mm, and the bubble formation efficiency is 0.5.

details are described in the Experimental procedures section, in which we also briefly compare our simulation with recently reported experimental data.[43] In short, two-dimensional (2D) multiphysics simulations are performed with a specific electrode length (channel length [L_y]) and gap between electrodes (channel width [L_x]). In our 2D model, we define the directions perpendicular and parallel to the channel flow as the x- and y-directions, respectively. The device tilt angle (θ) is defined as the angle between the y-direction (i.e., the device plane) and the horizontal orientation (see Figure 1A). Bubble formation efficiency (η_{bubble}) is introduced at the electrode surface. The produced bubbles are simulated by the Euler-Euler multiphase model, which calculates the volume fraction (α_i) and velocity vector ($\mathbf{v}_i$) of phase i (i.e., gas or liquid). The remaining products, $1-\eta_{bubble}$, are assumed to be dissolved gases, which are then treated using the transport of diluted species theory. All the symbols and parameters used in our simulations are shown in Tables S1 and S2, respectively. Unless specifically mentioned, the average applied current density,

electrode length, bubble diameter, and bubble formation efficiency are set to be 10 mA cm^{-2}, 10 cm, 0.1 mm, and 0.5, respectively. These values are chosen based on relevant recent experimental data using fluorine-doped tin oxide (FTO) electrode.[44] Although the bubble formation efficiency and its diameter may vary depending on the electrode materials,[45,46] we expect that the data measured with FTO are more relevant for solar fuel devices because it is often used as a substrate.

We first consider in this section a device configuration in which the anode is the upward-facing electrode (see Figure 1A for the definition of upward- and downward-facing electrodes). Bubbles produced at the downward-facing electrode (i.e., H$_2$ at the cathode in this case) remain very close to the electrodes due to gravity and therefore are not considered in our study. Figures 1B–1E show the simulated volume fraction of O$_2$ bubbles at 10 mA cm^{-2} for devices with different tilt angle θ. The inlet electrolyte velocity and the gap between electrodes were set to be 2.5 cm s^{-1} and 3 cm, respectively. The red arrows indicate the direction of gravity. When the electrodes are oriented vertically (θ = 90°; Figure 1B), O$_2$ bubbles remain close to the anode. As θ decreases (Figures 1C–1E), the bubble plume grows toward the middle of the cell, and it clearly crosses the middle of the cell when the device is in the horizontal orientation (θ = 0°). The interaction between the liquid and gas phase can be observed in the electrolyte's velocity profile, as shown in Figure S2. At regions very close to the inlet, a parabolic velocity profile is observed as expected for a single-phase laminar flow. The profile becomes distorted further away from the inlet due to the produced O$_2$ bubbles. This is caused by the momentum exchange between the liquid and gas phase, resulting in high velocity at regions close to the bubble-producing electrode, which further contributes to the mass transport of dissolved gases.

In order to evaluate the product crossover, we determine the molar flux profiles of O$_2$ bubbles and dissolved gases at the outlet for devices with various θ, as shown in Figures 2A–2C. As θ decreases, the flux of gas bubbles expands toward and even beyond the middle of the cell. At the same time, the fluxes of dissolved gases (both H$_2$ and O$_2$) also change following the respective velocity profiles (Figure S2); however, they remain close to the electrodes irrespective of θ. Our multiphase simulations therefore reveal that gas bubbles—often overlooked in previous reports[29,30]—contribute more significantly to the product crossover than dissolved gases in membrane-less, solar-driven water-splitting devices.

In our study, a divider is assumed to be located in the middle of the outlet (see Figure 1A and the dashed line at x = 0 in Figures 2A–2C). Such a divider has indeed been utilized in several membrane-less water-splitting devices.[19,20,43] Therefore, the product crossover is defined as the fraction of product fluxes that crosses beyond the middle of the outlet (i.e., $x > 0$ for O$_2$) against the total production. Figure 2D summarizes the product (O$_2$ in this case) crossover at different θ. The product crossover largely varies from 0 to more than 10%, depending on the orientation of the device. Similar to previous reports that only considered dissolved gases,[29,30] the average inlet velocity significantly affects the product crossover (Figure 2D). As an illustration, at θ = 30°, the product crossover can be suppressed by ~2 orders of magnitude from ~10% to ~0.1% by simply increasing the inlet velocity from 2 to 3 cm s^{-1}.

The prospect of introducing concentrated light, which reduces the area of semiconductors and electrodes with increased current density,[12,47] and its impact on the overall product crossover are also briefly considered. We varied the applied current
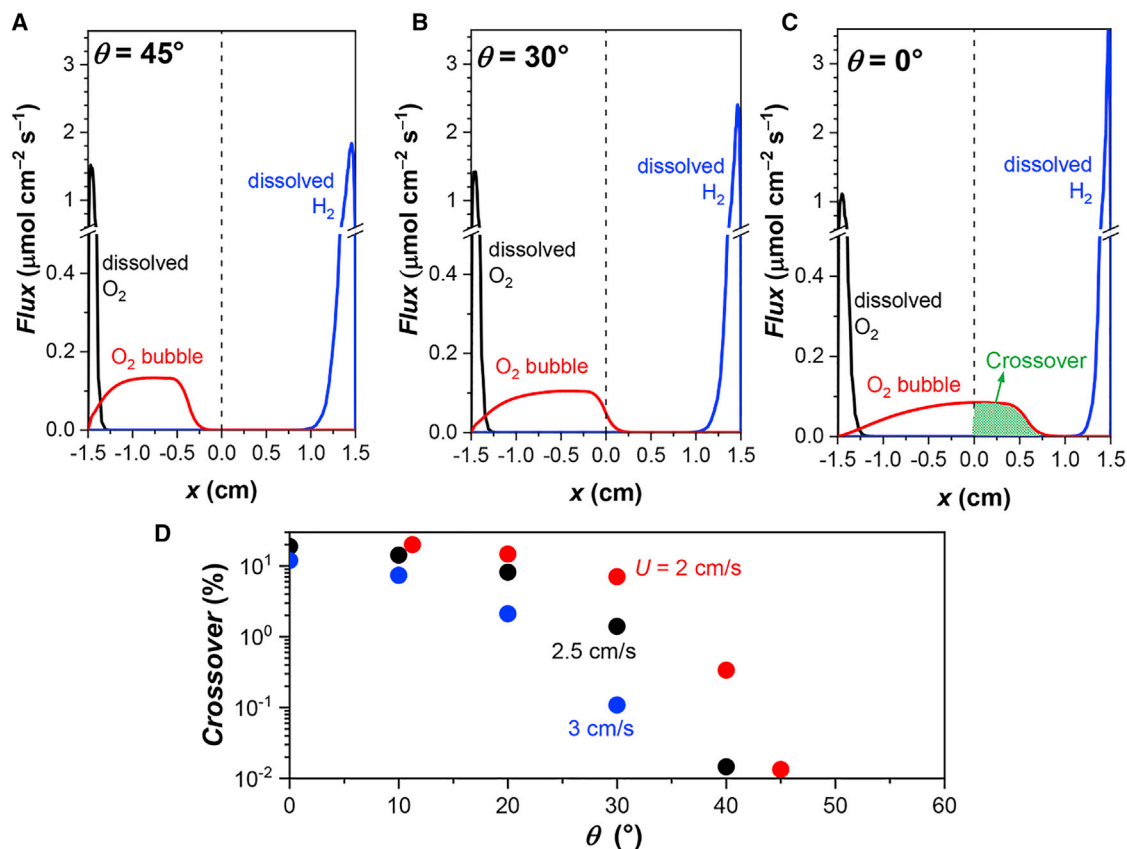
Figure 2. Flux profile at the outlet and the resultant product crossover at different tilt angles and inlet electrolyte velocity
(A–C) Flux profile of products at the outlet of devices tilted at different angles, θ = (A) 45°, (B) 30°, and (C) 0° (horizontal orientation). The average inlet velocity is kept constant at 2.5 cm s^{-1}.
(D) Crossover of product as a function of the device tilt angle θ for different inlet velocities. The average current density is 10 mA cm^{-2}, the bubble diameter is 0.1 mm, and the bubble formation efficiency is 0.5.

density while maintaining the total production rate over a square-shaped electrode, which means that the increased current density is accomplished by the reduction of electrode area and channel length. The crossover is found to be significantly suppressed with increasing the current densities (Figure S3), indicating a potential benefit of concentrated solar water splitting. This is because the channel length is reduced, which limits the distribution of gas bubbles within the channel before reaching the outlet. We note that the parameters of produced bubbles (i.e., bubble diameter and bubble formation efficiency) are kept constant in the present simulation for better comparison, but they are known to be dependent on the current density.[45,46,48,49] Detailed simulations that consider these factors are beyond the scope of our current study.

Sensitivity analysis of bubble characteristics

We now investigate the influence of the characteristics of gas bubbles on the overall product crossover. For instance, the bubble diameter, d, may vary depending on, e.g., the electrolyte flow rate, the surface tension of the electrolyte, and the hydrophobicity of the electrodes. Figures 3A–3C show the volume fraction of O_2 bubbles with different diameters at θ = 30°. As the bubble diameter decreases, the bubble plume stays closer to the electrode. This effect is a result of stronger momentum exchange between the electrolyte and the smaller gas bubbles, as expected from
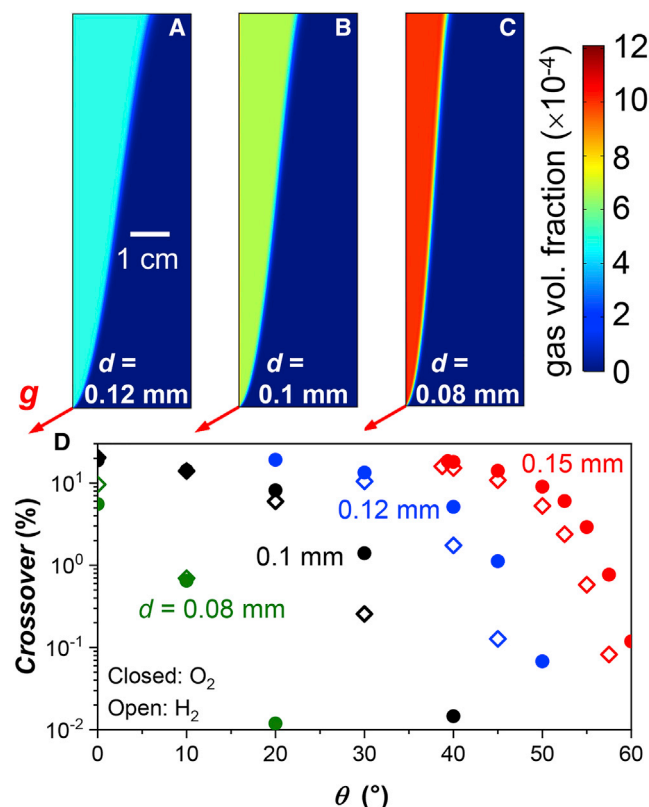
Figure 3. Influence of the characteristics of gas bubbles

(A–C) Colormaps of the volume fraction of O_2 bubbles with different bubble diameters ($\theta = 30°$). The bubble diameters considered are (A) 0.12, (B) 0.1, and (C) 0.08 mm. The red arrows indicate the direction of gravity.

(D) Crossover of O_2 and H_2 bubbles with different bubble diameters. The average liquid inlet velocity is 2.5 cm s^{-1}, the average current density is 10 mA cm^{-2}, and the bubble formation efficiency is 0.5.

See also Figure S4.

Equation 13 in Experimental procedures, which causes the gas phase velocity to follow that of the liquid phase toward the outlet. As a consequence, the product crossover can be significantly suppressed by reducing the bubble diameter, as shown in Figure 3D. The bubble break-off diameter at zero current, d_0, can be estimated, for example, using Fritz equation.[50,51]

$$d_0 = 1.14\vartheta \left\{ \frac{\Gamma}{g(\rho_L - \rho_G)} \right\}^{0.5},$$ (Equation 1)

where ϑ is the bubble contact angle and Γ is the surface tension. The bubble contact angle and the surface tension are often controlled by the modification of catalyst layers and introducing surfactants, respectively.[43,47,52–54] When surfactants are added, however, extra care has to be taken to avoid undesired (electro)chemical reactions of the surfactants at the electrodes. Nano-structuring of the electrode surface has also been reported to decrease the bubble diameter.[55–57]

The simulation results so far have only considered the anode as the upward-facing electrode, i.e., only O_2 bubbles were discussed. However, the product crossover may also be affected if we consider the cathode as the upward-facing electrode and H_2 bubbles limit the crossover. Therefore, we compare the production of O_2 and H_2 bubbles from the

upward-facing electrode. Figure 3D shows that, although no significant difference is observed for small θ, the crossover of H_2 is consistently lower than that of O_2 when θ is larger than 20°. In other words, in terms of product separation, it is beneficial to have the cathode as the upward-facing electrode. Two factors may contribute to the difference in the product crossover: (1) the different gas density, ρ_G, of H_2 and O_2 and (2) the number of electrons, n_e, involved in the electrochemical reactions. To identify their respective contributions, an imaginary gas with a density equal to that of H_2 but that requires 4 electrons in the electrochemical reaction is introduced. As shown in Figure S4A, the product crossover does not change when either O_2 or the imaginary gas is considered as the gas bubbles produced at the upward-facing electrode. This is caused by the negligible density difference between O_2 and H_2 as compared to the liquid density, ρ_L; the buoyancy force between the gas and liquid phase remains unaffected. The main contributing factor to the difference in the product crossover is therefore the number of electrons involved in the reaction, as evident from the difference between H_2 and the imaginary gas in Figure S4A. When an electrochemical reaction requires fewer electrons, the production of bubbles increases. Higher interaction between the bubbles and the liquid electrolyte is thus expected, which may increase the velocity close to the bubble-producing electrode. Indeed, as shown in Figure S4B, the velocity close to the bubble-producing electrode is higher when H_2 is produced instead of O_2 (or the imaginary gas) at $\theta = 30°$, which helps to suppress the product crossover. Note that such a velocity difference is not observed when the device is oriented horizontally, which agrees with the negligible change of product crossover when θ is below 20° (Figure 3D).

Another factor that may affect the overall product crossover is the bubble formation efficiency (η_{bubble}). Figure S5A shows the O_2 crossover as a function of θ for various values of η_{bubble}. The anode is again considered as the upward-facing electrode. At low θ range (<30°), the crossover increases as the bubble formation efficiency is increased. This is expected because higher η_{bubble} would increase the flux of O_2 bubbles, which determine the overall crossover (see Figures 2 and S5B). However, the trend is the opposite when θ is above 30°. This is initially surprising but can be explained if we closely examine the interaction between the gas bubbles and the liquid electrolyte. Similar to the comparison between H_2 and O_2 bubbles (vide supra), the higher η_{bubble} may increase the velocity of the electrolyte, especially at regions close to the bubble-producing electrode. Indeed, this is the case when θ is 30° (Figure S5C). Although the overall flux of O_2 bubbles is also increased (Figure S5D), the fraction that crosses beyond the middle of the outlet (i.e., $x > 0$) decreases because of the higher electrolyte velocity close to the electrode. Overall, our simulations above reveal that the interaction between the gas and liquid phase plays an important role to determine the electrolyte velocity and the resultant product crossover.

We finally note that, although the bubble diameter and bubble formation efficiency are parameterized here to understand their impacts, these parameters, in reality, are determined by the reaction conditions, such as current density, electrolyte flow rate, the surface tension of the electrolyte, and so on.[44,48,49,58–60] It is also likely that the values are not uniform across the surface of the electrodes, i.e., they are a function of the local environment. Future studies therefore require a detailed understanding of bubble nucleation, growth, and detachment to more accurately simulate the bubble diameter and the bubble formation efficiency at particular reaction conditions.

Design consideration for minimum power losses

In the previous sections, the gap between the electrodes (L_x) is maintained at 3 cm. Although it is preferable to reduce this gap to minimize the ohmic resistance of the
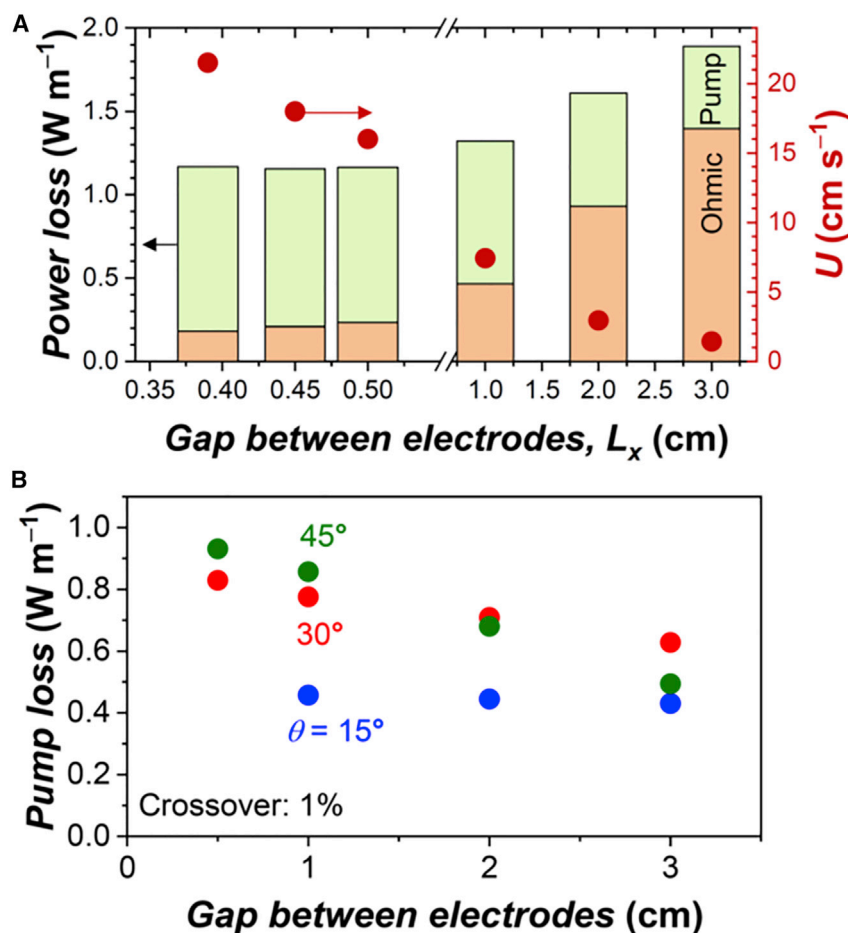
Figure 4. Trade-off between ohmic and pumping power losses
(A) Power losses in devices with different gap between electrodes, L_x, at $\theta = 45°$.
(B) Pumping power losses at different angles, θ. In all cases, the inlet liquid velocity, U, was optimized to obtain 1% crossover. See also Figure S6. The electrode and channel lengths are 10 cm, the average current density is 10 mA cm^{-2}, the bubble diameter is 0.1 mm, and the bubble formation efficiency is 0.5.

device, doing so would increase the product crossover. A higher inlet flow rate could be used to maintain the desired product crossover at the cost of higher pumping power. This inter-relation suggests that compensating factors are present, and optimum conditions may be found for minimal losses. Here, we compare the ohmic and pumping power losses, whose unit is W m^{-1} in 2D channel, to obtain a product crossover of 1%. The pump efficiency, η_{pump}, is assumed to be 0.6, based on the common value used in the literature.[29] The average inlet velocity, U, is then optimized individually for the different L_x in order to obtain a product crossover of 1%.

Figure 4A shows the ohmic and pumping power losses and the required inlet velocity to obtain 1% crossover with different electrode gaps, L_x. In this case, θ is kept at 45°. The ohmic power loss is proportional to L_x, although it is independent of the inlet liquid velocity and the device angle. At the same time, the required velocity to maintain 1% crossover significantly increases with narrower gaps, which increases the pumping power loss. As a consequence of this trade-off between the ohmic and pumping power losses, the optimal electrode gap (for this particular θ) is found to be

0.45 cm. The overall power loss (ohmic + pumping) of $\sim$1 W m^{-1} is $\sim$1% of the power input from the solar irradiation, which is still within an acceptable range.

The dependence of pumping power loss on θ is shown in Figure 4B. Two factors are contrasted that affect the pumping power loss: the required velocity to maintain 1% crossover and the pressure drop (Figure S6A). The former increases with decreasing θ, although the latter decreases. The competition between these two factors explains the maximum power loss observed at $\theta = 30°$ for larger L_x (>2 cm; see Figure 4B). Overall, the pumping power loss becomes more sensitive to the electrode gap with increasing θ due to the higher hydrostatic pressure difference. We note that the pressure drop in the channels also depends on the inlet velocity, the channel width, and the viscosity. However, its contribution ($\Delta p_{viscous}$) is negligible (<0.5%) as compared with the hydrostatic pressure (Figures S6A and S6B).

Because hydrostatic pressure difference largely contributes to the pumping power loss when the device is tilted away from the horizontal orientation, an alternative approach to reduce pressure drop is to flow the electrolyte toward the out-of-plane direction in our 2D model. Understanding the full extent of this potential solution, however, requires three-dimensional (3D) multiphase fluid simulations, which is beyond the scope of our current study.

Dimensionless analysis to obtain universal design criteria

Finally, in order to obtain a universal picture beyond the specific geometrical parameters and reaction conditions discussed above, a dimensionless analysis is introduced in this section. This analysis allows us to reduce the problem into several simple dimensionless numbers that characterize the behavior of our system. In the dimensional space, our multiphase fluid dynamics simulations contain ten variables and parameters to determine the volume fractions, the velocities, and the resultant fluxes of gas bubbles.

$$\{L_x, \ L_y, d, \rho_L, \rho_G, \mu_{mix}, U, \theta, R_G, g\Delta\rho\},$$

where R_G is the mass production rate of gas bubbles at the surface of the electrode. Dissolved gases are again ignored because they have a negligible contribution to the product crossover as discussed earlier (see Figure 2). For convenience, the density of gas, ρ_G, and the viscosity of mixture, μ_{mix}, are assumed to be constant because we found that their variations do not significantly impact our simulation results. Using the Buckingham Pi theorem,[61,62] we identify seven dimensionless numbers.

$$\{AR, \ \Pi_d, \Pi_\rho, \Pi_R, Fr, Ga, \theta\}$$

$$AR = \frac{L_y}{L_x} \quad \text{(Equation 2)}$$

$$\Pi_d = \frac{d}{L_x} \quad \text{(Equation 3)}$$

$$\Pi_\rho = \frac{\rho_G}{\rho_L} \quad \text{(Equation 4)}$$

$$\Pi_R = \frac{R_G}{\rho_L U} \quad \text{(Equation 5)}$$

$$Fr = \frac{U^2}{gL_x} = \frac{\text{(Inertia force)}}{\text{(Gravity)}} \quad \text{(Equation 6)}$$

$$Ga = \frac{g\rho_L^2 L_x^3}{\mu_{mix}^2} = \frac{Re^2}{Fr} = \frac{(Gravity)}{(Viscous\ force)} \qquad \text{(Equation 7)}$$

AR represents the aspect ratio, Π_d is the dimensionless bubble diameter, Π_ρ is the dimensionless density, and Π_R is the dimensionless bubble production rate, respectively. Froude (Fr) and Galilei (Ga) numbers compare the contributions from the inertia force, viscous force, and gravity. To check for consistency, we have also derived the same group of dimensionless numbers from the scaling of governing equations (see Note S2).

The obtained dimensionless parameters are validated using a case study in which the dimensional electrode length L_y is varied between 4 and 50 cm. The other dimensional parameters are adjusted so that all the dimensionless parameters are constant (see Table S3). Indeed, as long as all the dimensionless numbers are maintained, the same distribution of volume fraction and normalized fluxes at the outlet can be obtained (see Figure S7).

We then evaluate the universal design criteria to obtain 1% product crossover using the above-mentioned dimensionless numbers. As a further simplification of the problem, Π_ρ is kept constant at 1.3×10^{-3} because the density difference between gases is negligible as compared to the liquid density. We also note that the outputs of our dimensionless multiphase fluid dynamics simulations (e.g., the volume fractions, the normalized velocities, pressure, and the corresponding flux of gas bubbles) are independent of η_{bubble} as long as Π_R is maintained. Here, η_{bubble} is taken to be unity to simulate the extreme case of 100% bubble formation (i.e., no dissolved gases). In the realistic case that η_{bubble} is less than unity, implementing our design criteria of 1% crossover would actually result in an even smaller crossover (the exact value is $1 \times \eta_{bubble}$%). The present linear correction by η_{bubble} may seem to be in contradiction with Figure S5A, in which the relationship between crossover and η_{bubble} is not linear. This is because only the applied current density is maintained in the previous discussion, although the flux of gas bubbles is not maintained, as shown in Figures S5B and S5D. In this dimensionless analysis, however, the flux of gas bubbles is kept constant because the bubble production rate is used as an input parameter.

We first examine the critical Fr as a function of the dimensionless bubble production rate (Π_R). The critical Fr is relatively constant for $\Pi_R < 4.0 \times 10^{-7}$, but above this value, it decreases with increasing Π_R (Figure S8A). A closer look at the normalized liquid velocity profile (Figure S8B) reveals that bubbles start to strongly interact with the liquid phase and distort the profile for $\Pi_R > 4.0 \times 10^{-7}$. In contrast, below this critical Π_R value, the liquid velocity profile remains largely symmetric and parabolic, causing the critical Fr to be insensitive to Π_R; this is consistent with a previous report discussing the critical Peclet number for dissolved gases.[29] Similar dependence is also shown when the Ga number is modified from 3.0×10^6 to 2.4×10^7 (both values are relevant in our following discussions). Based on these results, we select a Π_R value from the relatively independent region (i.e., 1.1×10^{-7}) in the following discussions.

The relationship between the critical Fr and Ga to obtain 1% product crossover, while keeping the other dimensionless numbers constant, is shown in Figure 5A (black curve). Above and to the left of this curve, the product crossover is lower than 1%. This can be understood by taking Fr and Ga as indicators against gravity. In other words, Figure 5A essentially describes the criteria to overcome the buoyancy contribution in gaseous product separation. For instance, higher Fr, which can be obtained by, e.g., increasing the inlet velocity, represents stronger inertia
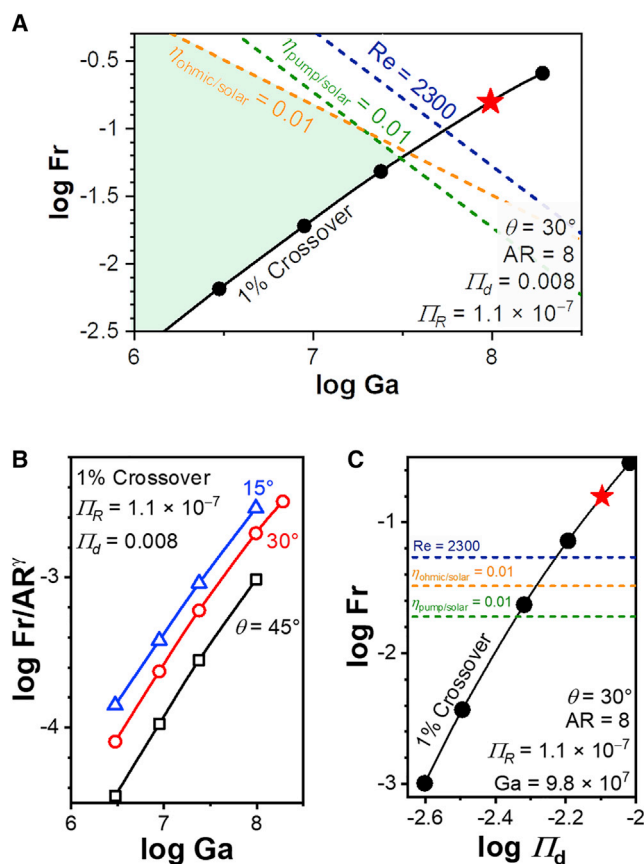
Figure 5. Design criteria with dimensionless numbers

(A) Critical Froude number and Galilei number to obtain 1% crossover while maintaining the other dimensionless parameters. The curve, combined with additional operational constraints of 1% ohmic loss ($\eta_{ohmic/solar}$), 1% pumping loss ($\eta_{pump/solar}$), and laminar flow condition (Reynolds number < 2,300), forms the operational design space indicated as the green-shaded region.

(B) Similar universal curves to (A) but independent of the aspect ratio, log Fr/AR$^{\gamma}$ versus log Ga, for various device tilt angle θ. See also Figures S9 and S10.

(C) Critical Froude number versus different dimensionless bubble diameters.

The red star points shown in (A) and (C) indicate identical conditions. The criteria for the critical Reynolds number to maintain laminar flow and pumping and ohmic power loss 1% are also shown in (C).

force, which minimizes the product crossover. Similarly, lower Ga (e.g., through decreasing the electrode gap) creates a sharp velocity gradient in the channel and a strong viscous force, which again reduces the crossover. This may initially seem to contradict our discussion in the previous section regarding the influence of the electrode gap. It should be noted, however, that the analysis in the previous section considers specific dimensional parameters, although in this case, the modification of Ga number is done while maintaining the other dimensionless numbers, such as AR and Π_d, constant.

In addition to the product crossover requirement, we introduce additional criteria to obtain acceptable device-operating conditions. First, both the ohmic and pumping losses in the device need to be minimized, ideally lower than 1%. In addition, because our multiphase model assumes laminar flow, a critical Reynolds number of 2,300 is added as another operational limit. These criteria are shown in Figure 5A as dashed lines (see Note S3 for the derivations of these criteria using dimensionless

descriptions and Table S4 for the benchmark operation conditions). The operational design space that satisfies all of our operational constraints is shown by the green-shaded region. Based on such analysis, a particular critical dimensional parameter (e.g., inlet velocity) can be easily calculated for various geometrical or operational parameters (e.g., electrode size and electrolyte).

The operational design space described above can of course be modified by varying the other dimensionless parameters. For example, increasing the AR would make the operational design space smaller (Figure S9). The orientation of the device (i.e., the device tilt angle [θ]) also affects the operational design space. Interestingly, a linear log-log dependence is observed at all θ between the critical Fr and the AR with a slope of γ, as shown in Figures S10A–S10D. Using this relationship, a universal curve independent of the aspect ratio, log Fr/AR$^{\gamma}$ versus log Ga, can be further derived for each θ value, as shown in Figure 5B. Higher θ shifts this curve down, i.e., it widens the operational design space. Finally, decreasing the Π_d, i.e., smaller bubble diameter or larger electrode gap, shifts the critical Fr to lower values, as shown in Figure 5C, such that all constraints can be satisfied.

In summary, the product crossover in solar-driven, membrane-less water-splitting devices has been thoroughly investigated using multiphase fluid dynamics simulations. As such devices will most likely be tilted for maximum sunlight exposure, various device orientations (i.e., tilt angles) have also been considered. Our simulations revealed that dissolved gases do not play a major part in determining product crossover. Instead, gas bubbles, often ignored in previous numerical studies, are the dominant contributor. We also showed that the overall product crossover is significantly influenced by the characteristics of the bubbles (bubble diameter, bubble formation efficiency, etc.). Notably, producing smaller bubbles improves product separation in the device. Further development of membrane-less water-splitting devices would therefore be benefited from a detailed understanding of bubble formation. Finally, we applied our multiphase model to perform an extensive dimensionless analysis. Based on such analysis, we identified several critical dimensionless numbers (e.g., Froude, Galilei number, and AR) and proposed the operational design space for minimal crossover. Overall, our study offers insights and provides universal design guidelines in the development of efficient solar-driven, membrane-less water-splitting devices.

EXPERIMENTAL PROCEDURES

Resource availability

Lead contact
Further information and requests for resources and reagents should be directed to and will be fulfilled by the lead contact, Fatwa F. Abdi (fatwa.abdi@helmholtz-berlin.de).

Materials availability
This study did not generate new unique materials.

Data and code availability
This study did not generate/analyze (datasets/code).

Model descriptions
Euler-Euler laminar flow model was used to simulate the multiphase fluid dynamics in our membrane-less, solar-driven water-splitting devices. Two sets of continuity and

momentum equations were solved using the volume fractions of the individual phases (Equations 8 and 9).

$$\frac{d(\alpha_i \rho_i)}{dt} + \nabla \cdot (\alpha_i \rho_i \boldsymbol{v}_i) = 0, \qquad \text{(Equation 8)}$$

$$\alpha_i \rho_i \left(\frac{d\boldsymbol{v}_i}{dt} + \boldsymbol{v}_i \cdot \nabla \boldsymbol{v}_i \right) = -\alpha_i \nabla p + \alpha_i \mu_{\text{mix}} \nabla^2 \boldsymbol{v}_i + \alpha_i \rho_i \boldsymbol{g} + \boldsymbol{F}_{i-j}, \qquad \text{(Equation 9)}$$

where α_i, ρ_i, and $\boldsymbol{v}_i$, represent the volume fraction, density, and velocity vector of phase i (L for liquid and G for gas), respectively. $\boldsymbol{g}$ denotes the gravity vector. μ_{mix} is the dynamic viscosity of the mixture (Equation 10).[63]

$$\mu_{\text{mix}} = \mu_{\text{L}}(1 - \alpha_{\text{G}})^{-2.5} \qquad \text{(Equation 10)}$$

The gravity vector in our 2D space was defined based on the device tilt angle, θ, and the gravitational acceleration constant, g:

$$\boldsymbol{g} = -g(\sin \theta, \cos \theta) \qquad \text{(Equation 11)}$$

The volume fractions of the liquid and gas phase are limited by the following Equation 12.

$$\alpha_{\text{L}} + \alpha_{\text{G}} = 1 \qquad \text{(Equation 12)}$$

The last term in Equation 9 ($\boldsymbol{F}_{i-j}$) is a momentum exchange term from phase j to i as described below.

$$\boldsymbol{F}_{\text{L-G}} = -\boldsymbol{F}_{\text{G-L}} = \frac{3}{4d} C_{\text{D}} \alpha_{\text{G}} \alpha_{\text{L}} \rho_{\text{L}} |\boldsymbol{v}_{\text{G}} - \boldsymbol{v}_{\text{L}}| (\boldsymbol{v}_{\text{G}} - \boldsymbol{v}_{\text{L}}) \qquad \text{(Equation 13)}$$

C_{D} and d represent the drag coefficient and the bubble diameter, respectively. Schiller-Naumann model was used to determine C_{D}.[64]

$$C_{\text{D}} = \begin{cases} \dfrac{24}{\text{Re}_{\text{p}}} \left(1 + 0.15 \text{Re}_{\text{p}}^{0.687} \right), & \text{Re}_{\text{p}} < 1000 \\ \\ 0.44 \quad, & \text{Re}_{\text{p}} \geq 1000 \end{cases},$$

in which Re_{p} denotes the particle Reynolds number.

$$\text{Re}_{\text{p}} = \frac{d\rho_{\text{L}} |\boldsymbol{v}_{\text{G}} - \boldsymbol{v}_{\text{L}}|}{\mu_{\text{mix}}} \qquad \text{(Equation 14)}$$

In the liquid phase, dilute-solution theory considering diffusive and convective mass transport was used for the dissolved O_2 and H_2.

$$\frac{\partial c_m}{\partial t} = -\nabla \cdot \boldsymbol{N}_m = -\nabla \cdot (-D_m \nabla c_m + c_m \boldsymbol{v}_{\text{L}}) = 0 \qquad \text{(Equation 15)}$$

$\boldsymbol{N}_m$, D_m, and c_m represent the flux vector, diffusion coefficient, and concentration of dissolved species m, respectively. Mass transfer between gas bubbles and dissolved gas was ignored.

At the electrode surface, the local current density (j_s) and the bubble formation efficiency (η_{bubble}) determined the velocity of gas bubbles (Equation 16), the mass flux of gas bubbles (Equation 17), and the molar flux of dissolved gases (Equation 18); all of these vectors were assumed to be perpendicular to the electrode surface (i.e., x-direction).

$$v_{\text{G},x} = \frac{j_s \eta_{\text{bubble}} M}{n_e F \rho_{\text{G}}}, \qquad \text{(Equation 16)}$$

$$R_{G,x} = \frac{j_s \eta_{bubble} M}{n_e F}, \qquad \text{(Equation 17)}$$

$$N_{m,x} = \frac{j_s (1 - \eta_{bubble})}{n_e F}, \qquad \text{(Equation 18)}$$

Where F, M, and n_e are Faraday constant, the molar mass of gas (O_2 or H_2), and the number of electrons involved in the reaction, respectively. In our study, due to gravity, the overall product crossover is limited by the bubbles generated at the upward-facing electrode. The bubbles from the downward-facing electrode easily accumulate on the electrode, which makes it difficult to solve because the present model only covers the above-mentioned inlet of gas bubbles and does not consider the interaction between the accumulated bubbles and the electrode. More advanced multiphase fluid dynamics simulations beyond the scope of this study, such as Euler-Lagrange, phase field, level set, and so on, are needed in order to fully cover the interaction between the accumulated bubbles and the downward-facing electrode; these simulations, however, require higher computational cost. Nevertheless, we managed to solve the fluid dynamics in the cell in which both the upward- and downward-facing electrodes are considered, for limited orientations ($\theta = 75°$–$90°$). Although the velocity profile varies due to the bubbles from the downward-facing electrode, the resultant flux of bubbles does not change significantly (Figure S11). Therefore, bubbles from the downward-facing electrode were not considered in this study.

In the present study, bubbles are assumed to be generated uniformly along the electrode surface, as shown in Equations 16, 17, and 18. As a comparison, we have also introduced nucleation sites as gas bubble inlets, whose length equals to the bubble diameter, uniformly distributed along the electrode. We assumed that the nucleation sites cover 10% of the electrode area estimated from a previous study,[65] and the total production rate of gas bubbles was maintained. Although the volume fraction of gas bubbles is localized close to the nucleation sites, it starts to distribute more uniformly toward the middle of the channel (Figure S12). Above 1% crossover, which is our criterion in this study, the difference is negligible when either uniform bubble generation or 10% of nucleation sites is considered. Moreover, below 1% crossover, implementing 10% nucleation sites results in an even smaller crossover. Therefore, to be more conservative, we assume that gas bubbles are generated uniformly along the electrode to simply the calculation.

A fully developed laminar flow was assumed at the electrolyte inlet.

$$v_{L,y} = 1.5U \left\{ 1 - \left(\frac{x}{L_x/2} \right)^2 \right\}, \qquad \text{(Equation 19)}$$

where U is the average inlet velocity. The concentration of dissolved gases and gas bubbles were set to be zero at the electrolyte inlet.

1 M KOH solution (ionic conductivity; $\sigma_0 = 0.215$ S cm^{-1})[66] was considered as the electrolyte. Due to the high concentration of OH$^-$, pH gradient during electrochemical reactions was assumed to be negligible.[67,68] Potential variations to the local conductivity of the electrolyte due to the presence of gas bubbles were initially considered based on the following Bruggeman correlation.[69]

$$\sigma = \sigma_0 (1 - \alpha_G)^{1.5} \qquad \text{(Equation 20)}$$

However, the Bruggeman-corrected local conductivity only resulted in a <0.1% variation of local current density as shown in Figure S13 (see also Note S1 and Figure S1C for the

description and schematic of the electrochemistry simulations), and there was no clear influence to the product crossover (not shown). In addition, the surface coverage of the electrode with gas bubbles may further vary the local current density along the electrode. The correlation between the two is not clear, but we speculate that the surface coverage is proportional to $(1-\alpha_G)^{1.5}$, similar to the above-mentioned Bruggeman correction. The term, $(1-\alpha_G)^{1.5}$, should be related to the electrochemically available cross-sectional area. However, as shown in Figure S13, the introduction of surface coverage did not vary the local current density distribution when the device is tilted away from the vertical orientation because of the small gas volume fraction. Even when the device is in vertical orientation, the variation is limited to ~3%. Furthermore, ohmic loss along the electrode may also change the local current density distribution, but we have previously simulated that this is largely dependent on the conductivity of the substrate and that it is negligible if potential mitigation strategies (e.g., the deposition of conductive metallic lines) are implemented;[30] this factor is not considered in the present study. Therefore, the local current density (j_s) was assumed to be uniform, which is equal to the applied current density (j_{app}). Similarly, the diffusion coefficients of dissolved species were also assumed to be constant and unaffected by the presence of gas bubbles.

A divider was assumed to be located in the middle of the outlet ($x = 0$, $y = L_y$ in Figure S1A). The molar fluxes for dissolved gases ($N_{m,y}$) and gas bubbles ($N_{G,y}$) in a direction normal to the outlet are described by Equations 21 and 22, respectively.

$$N_{m,y} = c_m v_{L,y} \qquad \text{(Equation 21)}$$

$$N_{G,y} = \alpha_G \rho_G v_{G,y}/M \qquad \text{(Equation 22)}$$

The crossover was determined by dividing the molar fluxes at $x \geq 0$ at the outlet with the overall electrochemical molar production rate from the entire electrode (Equation 23).

$$Crossover = \frac{\int_0^{L_x/2} (N_{G,y} + N_{m,y}) dx}{j_{app} L_y / n_e F} \qquad \text{(Equation 23)}$$

The power losses in 2D channel have the unit W m^{-1}. The ohmic power loss is independent of the inlet velocity and the device tilt angle as shown below.

$$P_{ohmic} = \frac{j_{app}^2 L_x L_y}{\sigma_0} \qquad \text{(Equation 24)}$$

The pumping power loss is described as follows.

$$P_{pump} = \frac{U L_x \Delta p}{\eta_{pump}}, \qquad \text{(Equation 25)}$$

where η_{pump} and Δp represent the efficiency of the pump and the pressure drop between the inlet and the outlet, respectively.

Steady-state simulations of the above equations were performed with COMSOL Multiphysics using PARDISO general solver. Relative tolerance of 0.005 was applied as the convergence criterion.

Our multiphase model is compared with a previous experimental study[43] as shown in Figure S14, which shows a relatively reasonable agreement. A slight underestimation of the crossover can be observed from our simulation, which may arise from either the distribution of bubble diameter or the interaction between bubbles and electrode/channel wall in a fully vertical orientation.

AUTHOR CONTRIBUTIONS

Conceptualization, K.O. and F.F.A.; methodology, K.O.; investigation, K.O. and A.M.; writing – original draft, K.O.; writing – review & editing, K.O. and F.F.A.; supervision, F.F.A.; funding acquisition, F.F.A.

DECLARATION OF INTERESTS

The authors declare no competing interests.

INCLUSION AND DIVERSITY

One or more of the authors of this paper self-identifies as an underrepresented ethnic minority in science.

REFERENCES

1. Cheng, W.-H., Richter, M.H., May, M.M., Ohlmann, J., Lackner, D., Dimroth, F., Hannappel, T., Atwater, H.A., and Lewerenz, H.-J. (2018). Monolithic photoelectrochemical device for direct water splitting with 19% efficiency. ACS Energy Lett. *3*, 1795–1800.

2. Young, J.L., Steiner, M.A., Döscher, H., France, R.M., Turner, J.A., and Deutsch, T.G. (2017). Direct solar-to-hydrogen conversion via inverted metamorphic multi-junction semiconductor architectures. Nat. Energy *2*, 17028.

3. Jia, J., Seitz, L.C., Benck, J.D., Huo, Y., Chen, Y., Ng, J.W.D., Bilir, T., Harris, J.S., and Jaramillo, T.F. (2016). Solar water splitting by photovoltaic-electrolysis with a solar-to-hydrogen efficiency over 30. Nat. Commun. *7*, 13237.

4. Nakamura, A., Ota, Y., Koike, K., Hidaka, Y., Nishioka, K., Sugiyama, M., and Fujii, K. (2015). A 24.4% solar to hydrogen energy conversion efficiency by combining concentrator photovoltaic modules and electrochemical cells. Appl. Phys. Express *8*, 107101.

5. Vilanova, A., Lopes, T., Spenke, C., Wullenkord, M., and Mendes, A. (2018). Optimized photoelectrochemical tandem cell for solar water splitting. Energy Storage Mater. *13*, 175–188.

6. Chen, Y., Hu, S., Xiang, C., and Lewis, N.S. (2015). A sensitivity analysis to assess the relative importance of improvements in electrocatalysts, light absorbers, and system geometry on the efficiency of solar-fuels generators. Energy Environ. Sci. *8*, 876–886.

7. Nurlaela, E., Shinagawa, T., Qureshi, M., Dhawale, D.S., and Takanabe, K. (2016). Temperature dependence of electrocatalytic and photocatalytic oxygen evolution reaction rates using NiFe oxide. ACS Catal. *6*, 1713–1722.

8. Haussener, S., Hu, S., Xiang, C., Weber, A.Z., and Lewis, N.S. (2013). Simulations of the irradiation and temperature dependence of the efficiency of tandem photoelectrochemical water-splitting systems. Energy Environ. Sci. *6*, 3605–3618.

9. Ye, X., Melas-Kyriazi, J., Feng, Z.A., Melosh, N.A., and Chueh, W.C. (2013). A semiconductor/mixed ion and electron conductor heterojunction for elevated-temperature water splitting. Phys. Chem. Chem. Phys. *15*, 15459–15469.

10. Vilanova, A., Lopes, T., and Mendes, A. (2018). Large-area photoelectrochemical water splitting using a multi-photoelectrode approach. J. Power Sources *398*, 224–232.

11. Chen, Y., Xiang, C., Hu, S., and Lewis, N.S. (2014). Modeling the performance of an integrated photoelectrolysis system with 10× solar concentrators. J. Electrochem. Soc. *161*, F1101.

12. Tembhurne, S., Nandjou, F., and Haussener, S. (2019). A thermally synergistic photo-electrochemical hydrogen generator operating under concentrated solar irradiation. Nat. Energy *4*, 399–407.

13. Rettie, A.J.E., Lee, H.C., Marshall, L.G., Lin, J.F., Capan, C., Lindemuth, J., McCloy, J.S., Zhou, J., Bard, A.J., and Mullins, C.B. (2013). Combined charge carrier transport and photoelectrochemical characterization of BiVO₄ single crystals: intrinsic behavior of a complex metal oxide. J. Am. Chem. Soc. *135*, 11389–11396.

14. Zhang, L., Ye, X., Boloor, M., Poletayev, A., Melosh, N.A., and Chueh, W.C. (2016). Significantly enhanced photocurrent for water oxidation in monolithic Mo:BiVO₄/SnO₂/Si by thermally increasing the minority carrier

diffusion length. Energy Environ. Sci. *9*, 2044–2052.

15. Ye, X., Yang, J., Boloor, M., Melosh, N.A., and Chueh, W.C. (2015). Thermally-enhanced minority carrier collection in hematite during photoelectrochemical water and sulfite oxidation. J. Mater. Chem. A *3*, 10801–10810.

16. Rettie, A.J.E., Chemelewski, W.D., Lindemuth, J., McCloy, J.S., Marshall, L.G., Zhou, J., Emin, D., and Mullins, C.B. (2015). Anisotropic small-polaron hopping in W:BiVO$_4$ single crystals. Appl. Phys. Lett. *106*, 022106.

17. Esposito, D.V. (2017). Membraneless electrolyzers for low-cost hydrogen production in a renewable energy future. Joule *1*, 651–658.

18. Modestino, M.A., Fernandez Rivas, D., Hashemi, S.M.H., Gardeniers, J.G.E., and Psaltis, D. (2016). The potential for microfluidics in electrochemical energy systems. Energy Environ. Sci. *9*, 3381–3391.

19. Talabi, O.O., Dorfi, A.E., O'Neil, G.D., and Esposito, D.V. (2017). Membraneless electrolyzers for the simultaneous production of acid and base. Chem. Commun. (Camb.) *53*, 8006–8009.

20. O'Neil, G.D., Christian, C.D., Brown, D.E., and Esposito, D.V. (2016). Hydrogen production with a simple and scalable membraneless electrolyzer. J. Electrochem. Soc. *163*, F3012.

21. Hashemi, S.M.H., Karnakov, P., Hadikhani, P., Chinello, E., Litvinov, S., Moser, C., Koumoutsakos, P., and Psaltis, D. (2019). A versatile and membrane-less electrochemical reactor for the electrolysis of water and brine. Energy Environ. Sci. *12*, 1592–1604.

22. Jin, J., Walczak, K., Singh, M.R., Karp, C., Lewis, N.S., and Xiang, C. (2014). An experimental and modeling/simulation-based evaluation of the efficiency and operational performance characteristics of an integrated, membrane-free, neutral pH solar-driven water-splitting system. Energy Environ. Sci. *7*, 3371–3380.

23. Davis, J.T., Qi, J., Fan, X., Bui, J.C., and Esposito, D.V. (2018). Floating membraneless PV-electrolyzer based on buoyancy-driven product separation. Int. J. Hydrogen Energy *43*, 1224–1238.

24. Davis, J.T., and Esposito, D.V. (2017). Limiting photocurrent analysis of a wide channel photoelectrochemical flow reactor. J. Phys. D Appl. Phys. *50*, 084002.

25. Hashemi, S.M.H., Neuenschwander, M., Hadikhani, P., Modestino, M.A., and Psaltis, D. (2017). Membrane-less micro fuel cell based on two-phase flow. J. Power Sources *348*, 212–218.

26. Da Mota, N., Finkelstein, D.A., Kirtland, J.D., Rodriguez, C.A., Stroock, A.D., and Abruña, H.D. (2012). Membraneless, room-temperature, direct borohydride/cerium fuel cell with power density of over 0.25 W/cm2. J. Am. Chem. Soc. *134*, 6076–6079.

27. Kjeang, E., Michel, R., Harrington, D.A., Djilali, N., and Sinton, D. (2008). A microfluidic fuel cell with flow-through porous electrodes. J. Am. Chem. Soc. *130*, 4000–4006.

28. Braff, W.A., Bazant, M.Z., and Buie, C.R. (2013). Membrane-less hydrogen bromine flow battery. Nat. Commun. *4*, 2346.

29. Holmes-Gentle, I., Hoffmann, F., Mesa, C.A., and Hellgardt, K. (2017). Membrane-less photoelectrochemical cells: product separation by hydrodynamic control. Sustain. Energy Fuels *1*, 1184–1198.

30. Abdi, F.F., Gutierrez Perez, R.R., and Haussener, S. (2020). Mitigating voltage losses in photoelectrochemical cell scale-up. Sustain. Energy Fuels *4*, 2734–2740.

31. Carver, C., Ulissi, Z., Ong, C.K., Dennison, S., Kelsall, G.H., and Hellgardt, K. (2012). Modelling and development of photoelectrochemical reactor for H$_2$ production. Int. J. Hydrogen Energy *37*, 2911–2923.

32. Carver, C., Ulissi, Z., Ong, C.K., Dennison, S., Hellgardt, K., and Kelsall, G.H. (2010). Modeling and evaluation of a photoelectrochemical reactor for H$_2$ production. ECS Trans. *28*, 103.

33. Jacobson, M.Z., and Jadhav, V. (2018). World estimates of PV optimal tilt angles and ratios of sunlight incident upon tilted and tracked PV panels relative to horizontal panels. Sol. Energy *169*, 55–66.

34. Liu, C.-L., Sun, Z., Lu, G.-M., and Yu, J.-G. (2018). Hydrodynamic characteristics of the two-phase flow field at gas-evolving electrodes: numerical and experimental studies. R. Soc. Open Sci. *5*, 171255.

35. Mat, M.D., and Aldas, K. (2005). Application of a two-phase flow model for natural convection in an electrochemical cell. Int. J. Hydrogen Energy *30*, 411–420.

36. Aldas, K., Pehlivanoglu, N., and Mat, M.D. (2008). Numerical and experimental investigation of two-phase flow in an electrochemical cell. Int. J. Hydrogen Energy *33*, 3668–3675.

37. Mat, M.D., Aldas, K., and Ilegbusi, O.J. (2004). A two-phase flow model for hydrogen evolution in an electrochemical cell. Int. J. Hydrogen Energy *29*, 1015–1023.

38. Alexiadis, A., Dudukovic, M.P., Ramachandran, P., Cornell, A., Wanngård, J., and Bokkers, A. (2011). Liquid-gas flow patterns in a narrow electrochemical channel. Chem. Eng. Sci. *66*, 2252–2260.

39. Taqieddin, A., Nazari, R., Rajic, L., and Alshawabkeh, A. (2017). Review-Physicochemical hydrodynamics of gas bubbles in two phase electrochemical systems. J. Electrochem. Soc. *164*, E448–E459.

40. Hreiz, R., Abdelouahed, L., Fünfschilling, D., and Lapicque, F. (2015). Electrogenerated bubbles induced convection in narrow vertical cells: a review. Chem. Eng. Res. Des. *100*, 268–281.

41. Mandin, P., Aissa, A.A., Roustan, H., Hamburger, J., and Picard, G. (2008). Two-phase electrolysis process: from the bubble to the electrochemical cell properties. Chem. Eng. Process. *47*, 1926–1932.

42. Mandin, P., Hamburger, J., Bessou, S., and Picard, G. (2005). Modelling and calculation of the current density distribution evolution at vertical gas-evolving electrodes. Electrochim. Acta *51*, 1140–1156.

43. Pang, X., Davis, J.T., Harvey, A.D., and Esposito, D.V. (2020). Framework for evaluating the performance limits of membraneless electrolyzers. Energy Environ. Sci. *13*, 3663–3678.

44. Holmes-Gentle, I., Bedoya-Lora, F., Alhersh, F., and Hellgardt, K. (2019). Optical losses at gas evolving photoelectrodes: implications for photoelectrochemical water splitting. J. Phys. Chem. C *123*, 17–28.

45. Vogt, H. (1984). The rate of gas evolution of electrodes—I. An estimate of the efficiency of gas evolution from the supersaturation of electrolyte adjacent to a gas-evolving electrode. Electrochim. Acta *29*, 167–173.

46. Chin Kwie Joe, J.M., Janssen, L.J.J., van Strelen, S.J.D., Verbunt, J.H.G., and Sluyter, W.M. (1988). Bubble parameters and efficiency of gas bubble evolution for a chlorine-, a hydrogen- and an oxygen-evolving wire electrode. Electrochim. Acta *33*, 769–779.

47. Khaselev, O., and Turner, J.A. (1998). A monolithic photovoltaic-photoelectrochemical device for hydrogen production via water splitting. Science *280*, 425–427.

48. Landolt, D., Acosta, R., Muller, R.H., and Tobias, C.W. (1970). An optical study of cathodic hydrogen evolution in high-rate electrolysis. J. Electrochem. Soc. *117*, 839.

49. Janssen, L.J.J., and Hoogland, J.G. (1973). The effect of electrolytically evolved gas bubbles on the thickness of the diffusion layer—II. Electrochim. Acta *18*, 543–550.

50. Fritz, W. (1935). Berechnung des maximalen Volumens von Dampfblasen. Phys. Z. *36*, 379–384.

51. Vogt, H. (2011). On the gas-evolution efficiency of electrodes. II – Numerical analysis. Electrochim. Acta *56*, 2404–2410.

52. Jiang, W., Yang, X., Li, F., Zhang, Q., Li, S., Tong, H., Jiang, Y., and Xia, L. (2019). Immobilization of a molecular cobalt cubane catalyst on porous BiVO$_4$ via electrochemical polymerization for efficient and stable photoelectrochemical water oxidation. Chem. Commun. (Camb.) *55*, 1414–1417.

53. Chen, B.-T., Morlanés, N., Adogla, E., Takanabe, K., and Rodionov, V.O. (2016). An efficient and stable hydrophobic molecular cobalt catalyst for water electro-oxidation at neutral pH. ACS Catal. *6*, 4647–4652.

54. Babu, R., and Das, M.K. (2018). Effects of surface-active agents on bubble growth and detachment from submerged orifice. Chem. Eng. Sci. *179*, 172–184.

55. Kempler, P.A., Coridan, R.H., and Lewis, N.S. (2020). Effects of bubbles on the electrochemical behavior of hydrogen-evolving Si microwire arrays oriented against gravity. Energy Environ. Sci. *13*, 1808–1817.

56. Lee, M.H., Takei, K., Zhang, J., Kapadia, R., Zheng, M., Chen, Y.Z., Nah, J., Matthews, T.S., Chueh, Y.L., Ager, J.W., and Javey, A. (2012). p-Type InP nanopillar photocathodes for efficient

solar-driven hydrogen production. Angew. Chem. Int. Ed. Engl. *51*, 10760–10764.

57. Li, Y., Zhang, H., Xu, T., Lu, Z., Wu, X., Wan, P., Sun, X., and Jiang, L. (2015). Under-water superaerophobic pine-shaped Pt nanoarray electrode for ultrahigh-performance hydrogen evolution. Adv. Funct. Mater. *25*, 1737–1744.

58. Angulo, A., van der Linde, P., Gardeniers, H., Modestino, M., and Fernández Rivas, D. (2020). Influence of bubbles on the energy conversion efficiency of electrochemical reactors. Joule *4*, 555–579.

59. Vogt, H., and Thonstad, J. (2017). The diversity and causes of current-potential behaviour at gas-evolving electrodes. Electrochim. Acta *250*, 393–398.

60. Vogt, H. (1989). Mechanisms of mass transfer of dissolved gas from a gas-evolving electrode and their effect on mass transfer coefficient and

concentration overpotential. J. Appl. Electrochem. *19*, 713–719.

61. Zlokarnik, M. (2006). Scale-up in Chemical Engineering (John Wiley & Sons).

62. Ruzicka, M.C. (2008). On dimensionless numbers. Chem. Eng. Res. Des. *86*, 835–868.

63. Enwald, H., Peirano, E., and Almstedt, A.-E. (1996). Eulerian two-phase flow theory applied to fluidization. Int. J. Multiph. Flow *22*, 21–66.

64. Shiller, L., and Naumann, A. (1935). A drag coefficient correlation. Zeitschrift des Vereins Dtsch. Ingenieure *77*, 318–320.

65. Balzer, R.J., and Vogt, H. (2003). Effect of electrolyte flow on the bubble coverage of vertical gas-evolving electrodes. J. Electrochem. Soc. *150*, E11.

66. Gilliam, R.J., Graydon, J.W., Kirk, D.W., and Thorpe, S.J. (2007). A review of specific

conductivities of potassium hydroxide solutions for various concentrations and temperatures. Int. J. Hydrogen Energy *32*, 359–364.

67. Shinagawa, T., Ng, M.T.K., and Takanabe, K. (2017). Electrolyte engineering towards efficient water splitting at mild pH. ChemSusChem *10*, 4155–4162.

68. Obata, K., van de Krol, R., Schwarze, M., Schomäcker, R., and Abdi, F.F. (2020). *In situ* observation of pH change during water splitting in neutral pH conditions: impact of natural convection driven by buoyancy effects. Energy Environ. Sci. *13*, 5104–5116.

69. Bruggeman, D.A.G. (1935). Berechnung verschiedener physikalischer Konstanten von heterogenen Substanzen. I. Dielektrizitätskonstanten und Leitfähigkeiten der Mischkörper aus isotropen Substanzen. Ann. Phys. *24*, 636–664.